



HAL
open science

Deep Focus Earthquakes: From High Temperature Experiments to Cold Slabs

Julien Gasc, Clémence Daigre, Arefeh Moarefvand, Damien Deldicque, Julien Fauconnier, Blandine Gardonio, Claudio Madonna, Pamela Burnley, Alexandre Schubnel

► **To cite this version:**

Julien Gasc, Clémence Daigre, Arefeh Moarefvand, Damien Deldicque, Julien Fauconnier, et al.. Deep Focus Earthquakes: From High Temperature Experiments to Cold Slabs. *Geology*, 2022, 50 (9), pp.1018-1022. 10.1130/G50084.1 . hal-03869555

HAL Id: hal-03869555

<https://ens.hal.science/hal-03869555>

Submitted on 2 Dec 2022

HAL is a multi-disciplinary open access archive for the deposit and dissemination of scientific research documents, whether they are published or not. The documents may come from teaching and research institutions in France or abroad, or from public or private research centers.

L'archive ouverte pluridisciplinaire **HAL**, est destinée au dépôt et à la diffusion de documents scientifiques de niveau recherche, publiés ou non, émanant des établissements d'enseignement et de recherche français ou étrangers, des laboratoires publics ou privés.

1 **Deep Focus Earthquakes: From High Temperature Experiments to**
2 **Cold Slabs**

3
4 Julien Gasc^{1*}, Clémence Daigre¹, Arefeh Moarefvand¹, Damien Deldicque¹, Julien Fauconnier¹,
5 Blandine Gardonio¹, Claudio Madonna², Pamela Burnley³ and Alexandre Schubnel¹

6
7 ¹*Laboratoire de Géologie CNRS-École Normale Supérieure, Paris, France.*

8 ²*ETH Zürich, Department of Earth Sciences, Zurich, Switzerland.*

9 ³*University of Nevada in Las Vegas, Department of Geoscience, Las Vegas NV, USA.*

10

11 **ABSTRACT**

12 Deep Focus Earthquakes (DFEs) present an interesting scientific challenge in that they occur at
13 depths where brittle failure should be impossible. The fact that their occurrence is confined to locations
14 where subducting lithospheric slabs are crossing through the transition zone suggests that the olivine phase
15 transformations may be involved in the production of these earthquakes. Experimental studies have shown
16 that olivine can persist metastably in subducting slabs and that the olivine phase transformations can lead
17 to faulting at high pressures. However, it has been argued that large DFEs are too large to be contained
18 within a metastable olivine wedge (MOW) preserved in the interior of subducting slabs. Here, we
19 demonstrate using experiments on olivine-analog materials that transformational faulting can continue to
20 propagate via shear-enhanced melting into the stable high-pressure phase. We also show that
21 transformational faulting is controlled by the ratio between strain rate and the kinetics of the olivine-
22 ringwoodite transformation and extrapolate this relationship to the natural conditions of DFEs.
23 Counterintuitively, these results imply that cold and fast-subducting slabs produce transformational
24 faulting at higher temperatures, which results in more numerous DFEs.

26 **INTRODUCTION**

27 A century after their discovery, the mechanisms responsible for DFEs are still highly debated (Luo
28 and Wiens, 2020; Turner, 1922). The olivine-ringwoodite transformation was proven to cause brittle
29 behavior (i.e., transformational faulting) at conditions where ductile deformation otherwise prevails
30 (Burnley et al., 1991). It can also explain the anomalously high DFE activity in Tonga, which has been
31 attributed to the thermal state of the subducting slab, colder slabs allowing for the preservation of more
32 metastable olivine (Green, 2007; Kirby et al., 1996). Yet, large DFEs do not only occur in the coldest slabs
33 and the large productivity of Tonga is due to a uniquely large proportion of small earthquakes (Frohlich,
34 2006; Houston, 2015; Wiens, 2001). These differences have been attributed to the geometry of the MOW,
35 where transformational faulting occurs (Zhan, 2020). On the other hand, transformational faulting has been
36 contested as the origin for DFEs due to the fact that the fault dimension of major DFEs is larger than that
37 of the MOW (Wiens, 2001). It has been proposed that large DFEs may initiate within the MOW via
38 transformational faulting, and then propagate outside of it via thermal runaway processes (Zhan, 2017;

39 (McGuire et al., 1997). However, experimental data exploring the conditions necessary for
40 transformational faulting in terms of transformation kinetics, as well as testing the possible propagation in
41 ringwoodite peridotites are still lacking. In this paper, we address these outstanding questions.

42 The seminal work of Burnley, Green and co-authors regarding transformational faulting used a
43 germanium olivine (Ge-Olivine) analogue, a material that undergoes the transition to the ringwoodite
44 structure (Ge-spinel) at much lower pressures than the silicate counterpart (Burnley and Green, 1989;
45 Burnley et al., 1991; Green and Burnley, 1989; Schubnel et al., 2013; Wang et al., 2017). Here we
46 continue to build upon this work by combining high pressure deformation experiments with acoustic
47 emission (AE) monitoring. Ge-olivine samples were deformed in the Ge-spinel field at 1.5 GPa in a
48 modified Griggs apparatus (Moarefvand et al., 2021). The experiments investigate lower temperatures and
49 strain rates to assess the extrapolation of transformational faulting towards natural conditions and test the
50 possibility of fault propagation into fully transformed material.

51 **RESULTS**

53 **Mechanical Behavior and Microseismicity**

54 The experiments display a range of transformation and deformation behavior (Figure 1 and
55 supplementary table 1). At the highest temperature, samples are nearly fully transformed (DU1F, 843°C
56 and DU2S, 834°C) with differential stress remaining below the confining pressure (1.5 GPa). Both
57 samples exhibited a softening behavior beyond peak stress. In DU2S performed at the lowest strain rate, no
58 AE was detected during deformation, whereas for DU1F, the softening phase was associated with a large
59 burst of small AEs.

60 All experiments performed at lower temperatures (506-703°C) lead to sample failure. The degree
61 of transformation ranged from 1 - 20% depending on both temperature and time at temperature. Three
62 experiments were performed at 703°C, including TF2F, where a shorter Ge-olivine sample was
63 sandwiched between two smaller Ge-spinel samples. Aside from this latter experiment, ultimate failure of
64 the sample occurred at lower strains at higher temperatures, inconsistent with normal brittle failure. This is

65 clear when comparing the stress-strain curves of TF1F and TF3S (703°C) to that of BR1F (506°C), which
66 displayed a stress plateau before eventual failure.

67 Despite attaining similar strengths before failing, the AE records from the 703°C experiments were
68 remarkably different than those obtained at lower temperatures, where fewer AEs were detected (32 at
69 609°C and 7 at 506°C), consistently with the increase of ductility towards lower temperatures.
70 Furthermore, at 703°C, the largest number of AEs, 633, was obtained at the slowest strain rate investigated
71 (TF3S), where failure occurred by a series of stick-slip events rather than by a major stress drop. The
72 number of AEs is comparable in DU1F, conducted at faster strain rates and higher temperature (843°C,
73 Figure 1b).

74 Interestingly, despite more numerous AEs during DU1F and TF3S (843 and 703°C), the
75 cumulative RMS—a proxy for magnitude—for these experiments is much lower than that of TF1F and
76 TF2F at 703°C and BR2S at 609°C (Figure 1c). In other words, AEs were less numerous at faster strain
77 rates or lower temperatures but had much larger amplitudes. In summary, experiments BR1F (506°C) and
78 DU2S (834°C) represent two end members of the mechanical behavior spectrum encompassed here. In
79 both cases, the samples exhibited ductility accompanied by a few AEs at most. In all other experiments,
80 AEs and/or brittle failure was observed, thus defining a transformational faulting temperature window,
81 where the most acoustic energy was detected.

82 The magnitude-frequency distribution of AEs obeys the same classical Gutenberg-Richter relation
83 as earthquakes, where the b -value reflects the topological dimension of the region where faults propagate
84 (Aki, 1981; Gasc et al., 2017; Gutenberg and Richter, 1949; Riviere et al., 2018). At 703°C, faulting yields
85 low b -values, whereas it is unequivocally higher at 843°C. In particular, the comparison between TF3S
86 and DU1F, which both produced ~ 600 AEs, yields striking differences, with $b = 0.62$ and $b = 1.5$,
87 respectively (Figure S3). At high temperature, wide and fully reacted mylonitic shear bands developed
88 (Figure 2c-d). This suggests that the small numerous AEs that accompany the growth of the shear bands
89 are grain-scale cracks distributed in a volume. At $\leq 703^\circ\text{C}$, on the other hand, deformation was
90 accommodated along sharp faults and narrow shear bands (Figure 2a-b), which is consistent with a lower

91 *b*-value and AEs being confined to smaller topological dimensions, typically in linear-to-planar features
92 (i.e., strips; see supplementary information).

93 **Dynamic Fault Propagation**

94 Sample TF2F contains a sharp fault that propagated through Ge-olivine and Ge-spinel alike
95 (Figure 2a). This sample was deformed under the same conditions as TF1F and failed at similar stress
96 levels, radiating nearly identical amounts of energy (Figure 1). Microstructures are also similar to those of
97 TF1F. It is therefore likely that this sample also failed by transformational faulting before the fault
98 propagated through Ge-spinel. Evidence for melt is present along the fault as stretches of very fine-grained
99 material (Figure 2b, Figure S4) with grain size gradients consistent with fast static recrystallization. These
00 observations suggest that co-seismic slip at high pressure is accompanied by frictional melting. As an
01 analogue to Nature, experiment TF2F is crucial because it is a strong indication that transformational
02 faulting events in the MOW may propagate as larger earthquakes in the adjacent ringwoodite peridotites
03 (McGuire et al., 1997).

04 05 **DISCUSSION**

06 **Transformational faulting, from laboratory to subducting slab**

07 Our results demonstrate a clear shift towards lower temperatures of the transformational faulting
08 temperature window previously described at faster strain rates (Burnley et al., 1991; Schubnel et al., 2013).
09 Transformational faulting is controlled by the transformation kinetic. If the transformation proceeds
10 quickly enough, relative to the imposed strain rate, ductile shear prevails. Thus, the weakening observed at
11 high temperature is likely due to the transformation relieving stress in two ways. First, the growth of fine-
12 grained products induces a weakening (Mohiuddin et al., 2020; Rutter and Brodie, 1988). Second, the
13 negative volume change accompanying the transformation accommodates the imposed compressive strain
14 (Incel et al., 2019).

15 On the other hand, if the transformation is sluggish or entirely hindered by the nucleation barrier,
16 deformation is also ductile but accommodated by plastic deformation of the metastable olivine and stress
17 levels are much higher. Transformational faulting corresponds to an intermediate scenario in which the

18 stress evolution is initially governed by the strength of olivine but due to the transformation, regions that
19 are mechanically unstable grow and coalesce, triggering the eventual failure. We propose that the
20 boundaries between faulting and low and high temperature ductile behavior can be plotted in strain rate -
21 transformation rate space in order to extrapolate the faulting window to Earth conditions (Figure 3a).
22 Faulting was observed here at grain growth and strain rates both 1-2 orders of magnitude lower than in
23 previous studies (Burnley et al., 1991; Schubnel et al., 2013). The resulting trend is remarkably consistent
24 with a slope of one in a log-log plot. Furthermore, transformational faulting of fayalite and natural olivine
25 plot along the same trend, which illustrates the universal nature of this mechanism (Green et al., 1990;
26 Officer and Secco, 2020). With the temperature dependence taken here ($E = 250 \text{ kJ mol}^{-1}$, see supp mat),
27 extrapolating to subduction zone strain rates predicts a transformational faulting window in the range of
28 600-700°C for strain rates of $\sim 10^{-11} \text{ s}^{-1}$ (Figure 3b), consistently with estimated temperatures of DFEs
29 (Kirby et al., 1996).

30 To illustrate how kinetics vs strain rate behavior plays out in subducting slabs, we consider two
31 endmember cases; Bolivia and Tonga. Bolivia has a low thermal parameter ($\phi \propto \text{plate age at trench} \times$
32 convergence rate) of 1800 km, whereas Tonga combines a record high thermal parameter of 14000 km and
33 the largest population of DFEs (Syracuse et al., 2010). Thermal structures for these subduction parameters
34 are shown in Figure 4 (King et al., 2020; van Keken et al., 2008). As expected, the high thermal parameter
35 case (fast slab) implies a tremendous thermal anomaly. The lowest temperature at the top of the transition
36 zone is 360°C, whereas it is $\sim 650^\circ\text{C}$ in the slow slab.

37 Assuming that strain rates are proportional to the descent rate, the resulting strain rate and
38 temperature conditions are plotted in Figure 3b with the intersection between the transformation faulting
39 window and slab conditions being enclosed with dashed lines. The region corresponding to the faster
40 subducting slab plots at lower temperatures and higher strains rates by a factor of three, corresponding to
41 the ratio of descent rate (Billen, 2020). As a consequence, in the more sluggish slab, DFEs occur in a
42 narrower temperature window. In addition, the coldest part of the fast slab is predicted to remain strong
43 and ductile, (i.e., aseismic) due to sluggish kinetics (Yoshioka et al., 2015). An important and

44 counterintuitive result that also emerges from the difference in strain rate is that transformational faulting
45 may take place at higher temperature (by $\sim 60^\circ\text{C}$) in the colder slab.

46 **Magnitude-Frequency Distributions**

47 The b -value difference between Bolivia and Tonga (0.5 and 1.1, respectively) can therefore be
48 predicted by our results, which show a dramatic b -value increase from 0.6 to 1.5 for a temperature increase
49 of 140°C (Figure S3). The higher b -value reflects the larger number of events that occur at high
50 temperature. Thus, not only is more of the fast slab in the transformation faulting window but it also
51 includes a hotter region that produces more small earthquakes and a higher b -value.

52 It has been suggested that the lower b -value in the case of Bolivia reflects the narrow nature of the
53 MOW (Zhan, 2017). However, the transformational faulting regions are predicted to be of similar width
54 for the Tonga and Bolivia analogues, due to a larger temperature window but a tighter distribution of
55 isotherms in the former (Figure 4d). The present results imply that the core of the fast slab remains
56 unreacted and that DFEs form a double seismic zone in the olivine-ringwoodite transformation fronts
57 surrounding the MOW (Wiens et al., 1993). The higher b -value in Tonga reflects a higher temperature of
58 transformational faulting, which triggers a myriad of low-magnitude earthquakes, with a small size relative
59 to the dimensions of the region in which they occur.

60 In conclusion, we have demonstrated that transformational faulting is controlled by the ratio
61 between transformation rates and strain rates, which predicts the occurrence of DFEs under subduction
62 zone strain rates. Finally, our study answers the most serious challenge confronting the transformational
63 faulting hypothesis; that the dimensions of the largest DFEs exceed those of the MOW. The fact that
64 sample TF2F contained a fault that propagated into and across the Ge-spinel portions of the sample shows
65 that once dynamic failure is initiated it can propagate beyond the boundaries of the metastable material.
66 Even within the boundaries of our millimeter scale samples, conditions are sufficient to produce frictional
67 melting. Similar shear enhanced melting can be expected in the mantle.

68 **Acknowledgments**

69 This project has received funding from the ERC grant REALISM (No. 681346)
70 and from the MELODIES grant of the TelluS program of CNRS/INSU. The authors
71 benefited from fruitful discussions with Harsha Bhat, and from Yves Pinquier’s technical
72 support. We thank Douglas Wiens and an anonymous reviewer for providing very helpful
73 reviews.
74

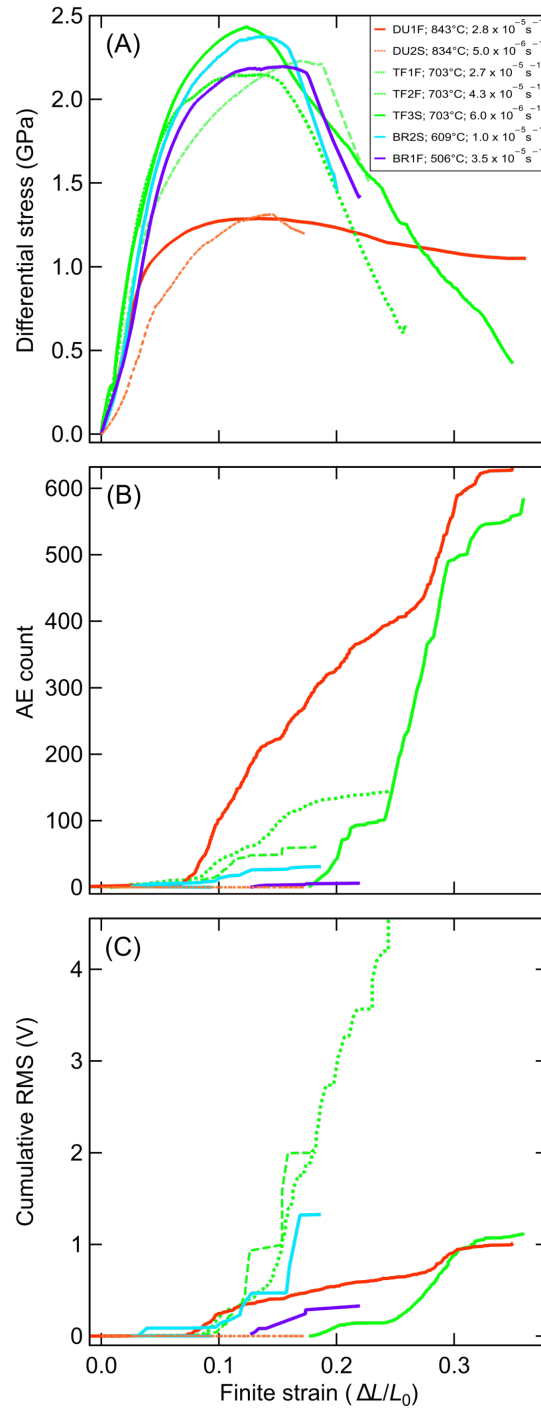


Fig. 1. Mechanical and Acoustic data. Data were color-coded according to temperature (506-843°C). (A) Evolution of differential stress with sample shortening. The names and strain rates of the experiments are given in the inset. The first two letters, DU, TF or BR stand for ductile, brittle and transformational faulting, respectively. The last letter, F or S, denotes a relatively fast or slow strain rate. (B) and (C) Cumulative number of AEs and RMS. No AE was detected for DU2S, which is represented by a horizontal line at 0 in (B) and (C).

76
77
78
79
80
81
82
83
84
85
86
87

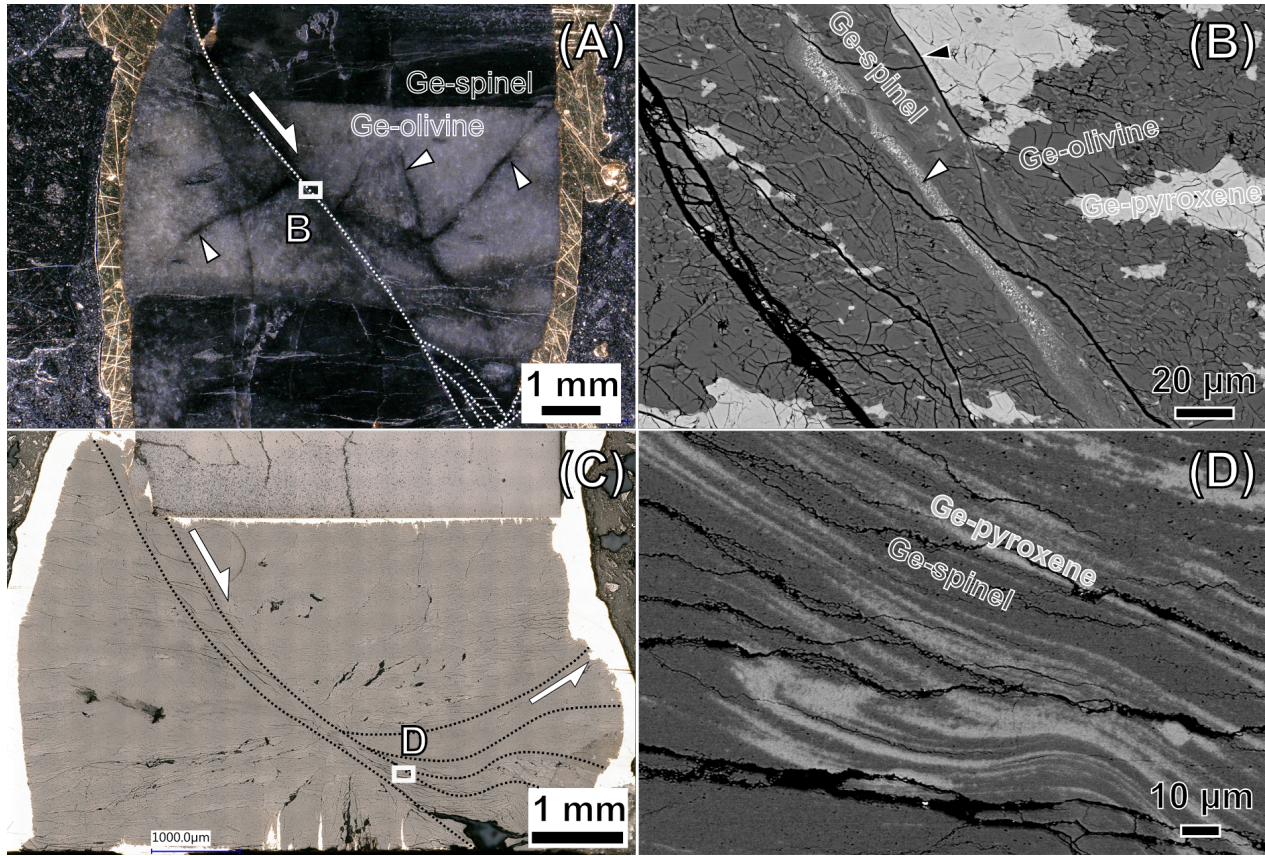


Fig. 2. Images of samples TF2F and DU1F. (A) Optical image of sample TF2F (703°C). Ge-spinel cores appear darker above and below the Ge-olivine in which reacted regions appear darker (arrowheads). A fault offsets all three parts (dashed lines and half-headed arrow). The horse-tail feature is indicative of rupture deceleration. (B) SEM image of the region shown by the rectangle in (A). The brighter phase is Ge-pyroxene, Ge-olivine is dark gray. The fault plane is evidenced by the sharp offset of a Ge-pyroxene grain (black arrowhead). Ge-spinel appears brighter; it is ubiquitous along the fault and present as lenses throughout the whole image. A stretch of small grains with important grain size gradients (white arrowhead) evidences that dynamic slip was accompanied by melting (see Figure S4 for detail). (C) Optical image of sample DU1F (843°C). Shear bands are observed (dashed curves). The main shear band is 100-350 μm wide. (D) SEM image corresponding to the rectangle in (C). Shearing is evidenced by dramatic Ge-pyroxene dynamic recrystallization.

88
89
90
91
92
93
94
95
96
97
98
99
00
01
02
03
04
05
06
07
08
09
10
11
12
13
14
15

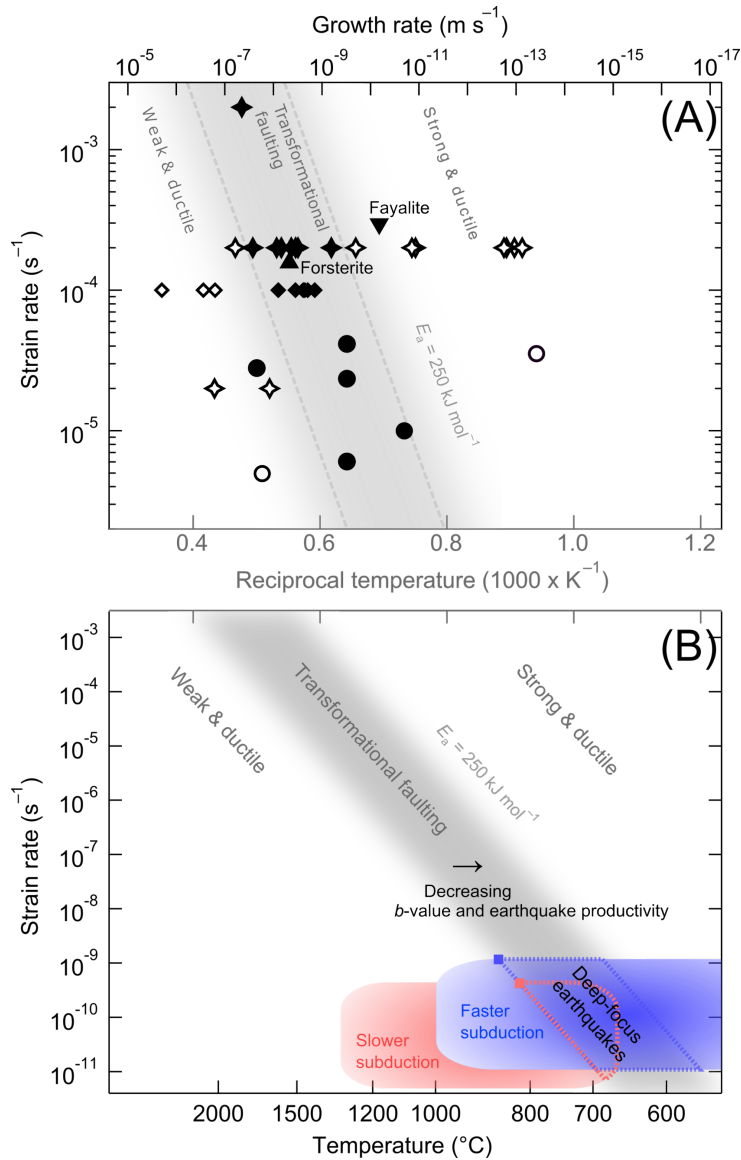


Fig. 3. Transformational faulting as a function of strain and grain growth rates.

Horizontal axis is the same on both panels. (A) Deformation conditions of Mg_2GeO_4 are represented by diamonds, stars and circles for Schubnel et al. (2013), Burnley et al. (1991) and the present study, respectively. Faulting is indicated by full symbols; open symbols indicate ductile behavior. Up- and down-pointing triangles represent transformational faulting for natural forsterite (Green et al., 1990) and fayalite (Officer and Secco, 2020), respectively. The bottom axis shows the equivalent reciprocal temperature calculated from the grain growth law of (Perrillat et al., 2016) for natural olivine. (B) Extrapolation of the transformational faulting window. The blue and red boxes represent conditions for two subducting slabs (see text for details). The overlaps between these rectangles and the transformational faulting window thus depict conditions under which DFEs may occur. The blue and red symbols mark the highest temperature of transformational faulting.

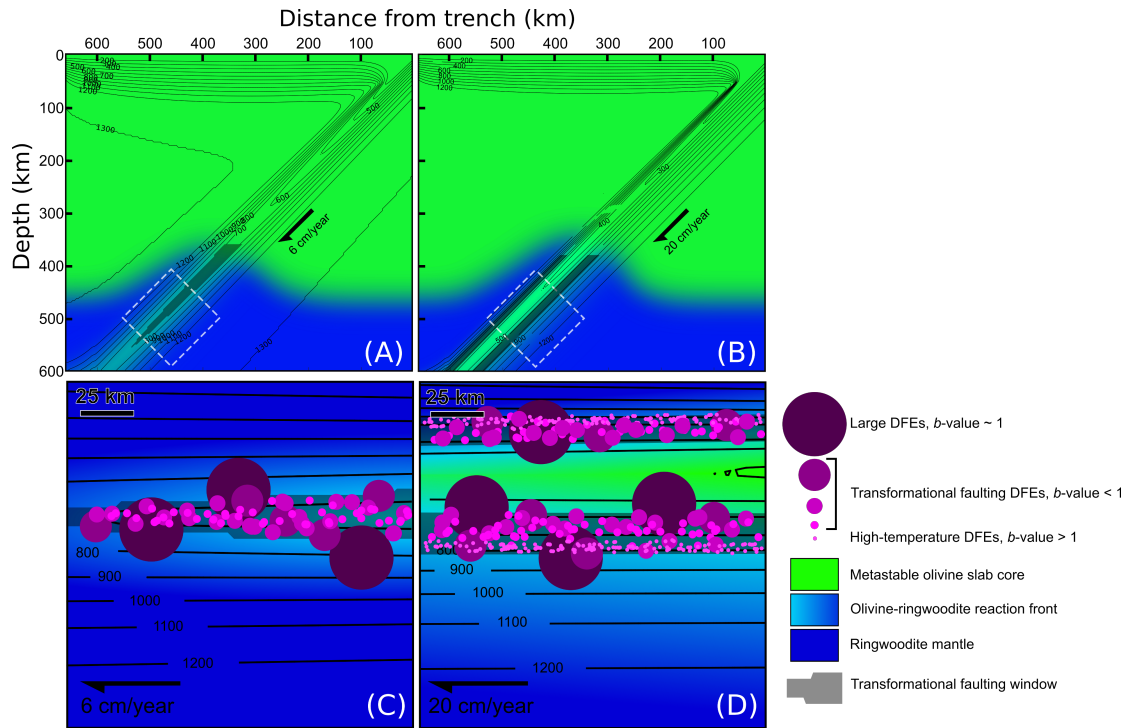


Fig. 4. Thermal slab structures and their relations to DFEs. (A) and (B) show thermal distributions for thermal parameters of Bolivia and Tonga, respectively. Isotherms were plotted every 100°C. (C) and (D) are magnified views according to the dashed squares in (A) and (B), respectively. The transformational faulting window is represented by the shadowed area (see text for details). Circles represent the locations and magnitudes of DFEs. Although earthquakes are triggered by transformational faulting, the largest events may propagate either in adjacent ringwoodite mantle or in cold metastable olivine. The faster slab presents an additional population of small earthquakes at higher temperature resulting in a lower b -value.

- 47
48 Aki, K., 1981, A Probabilistic Synthesis of Precursory Phenomena, *Earthquake Prediction*, p. 566-574.
- 49 Billen, M. I., 2020, Deep slab seismicity limited by rate of deformation in the transition zone: *Science Advances*, v.
50 6, no. 22, p. eaaz7692.
- 51 Burnley, P. C., 1995, The fate of olivine in subducting slabs: A reconnaissance study: *American Mineralogist*, v. 80,
52 no. 11-12, p. 1293-1301.
- 53 Burnley, P. C., and Green, H. W., 1989, STRESS DEPENDENCE OF THE MECHANISM OF THE OLIVINE
54 SPINEL TRANSFORMATION: *Nature*, v. 338, no. 6218, p. 753-756.
- 55 Burnley, P. C., Green, H. W., and Prior, D. J., 1991, FAULTING ASSOCIATED WITH THE OLIVINE TO SPINEL
56 TRANSFORMATION IN MG₂GEO₄ AND ITS IMPLICATIONS FOR DEEP-FOCUS EARTHQUAKES:
57 *Journal of Geophysical Research-Solid Earth and Planets*, v. 96, no. B1, p. 425-443.
- 58 Frohlich, C., 2006, *Deep Earthquakes*, Cambridge University Press.
- 59 Gasc, J., Hilairret, N., Yu, T., Ferrand, T., Schubnel, A., and Wang, Y., 2017, Faulting of natural serpentinite:
60 Implications for intermediate-depth seismicity: *Earth and Planetary Science Letters*, v. 474, p. 138-147.
- 61 Green, H. W., 2007, Shearing instabilities accompanying high-pressure phase transformations and the mechanics of
62 deep earthquakes: *Proceedings of the National Academy of Sciences of the United States of America*, v.
63 104, no. 22, p. 9133-9138.
- 64 Green, H. W., and Burnley, P. C., 1989, A NEW SELF-ORGANIZING MECHANISM FOR DEEP-FOCUS
65 EARTHQUAKES: *Nature*, v. 341, no. 6244, p. 733-737.
- 66 Green, H. W., Young, T. E., Walker, D., and Scholz, C. H., 1990, ANTICRACK-ASSOCIATED FAULTING AT
67 VERY HIGH-PRESSURE IN NATURAL OLIVINE: *Nature*, v. 348, no. 6303, p. 720-722.
- 68 Gutenberg, B., and Richter, C., 1949, *Seismicity of the earth and associated phenomena*, Princeton, New Jersey.
- 69 Houston, H., 2015, *Deep Earthquakes*, p. 329 - 354.
- 70 Incel, S., Labrousse, L., Hilairret, N., John, T., Gasc, J., Shi, F., Wang, Y. B., Andersen, T. B., Renard, F., Jamtveit,
71 B., and Schubnel, A., 2019, Reaction-induced embrittlement of the lower continental crust: *Geology*, v. 47,
72 no. 3, p. 235-238.
- 73 King, S., Raefsky, A., and Hager, B. H., 2020, ConMan version 3.0.0, Zenodo.
- 74 Kirby, S. H., Stein, S., Okal, E. A., and Rubie, D. C., 1996, Metastable mantle phase transformations and deep
75 earthquakes in subducting oceanic lithosphere: *Reviews of Geophysics*, v. 34, no. 2, p. 261-306.
- 76 Luo, Y. T., and Wiens, D. A., 2020, High Rates of Deep Earthquake Dynamic Triggering in the Thermal Halos of
77 Subducting Slabs: *Geophysical Research Letters*, v. 47, no. 8.
- 78 McGuire, J. J., Wiens, D. A., Shore, P. J., and Bevis, M. G., 1997, The March 9, 1994 (M-w 7.6), deep Tonga
79 earthquake: Rupture outside the seismically active slab: *Journal of Geophysical Research-Solid Earth*, v. 102, no. B7,
80 p. 15163-15182.
- 81 Moarefvand, A., Gasc, J., Fauconnier, J., Baïssset, M., Burdette, E., Labrousse, L., and Schubnel, A., 2021, A new
82 generation Griggs apparatus with active acoustic monitoring: *Tectonophysics*, v. 816, p. 229032.
- 83 Mohiuddin, A., Karato, S., and Girard, J., Slab weakening during the olivine to ringwoodite transition in the mantle:
84 *Nature Geoscience*.
- 85 -, 2020, Slab weakening during the olivine to ringwoodite transition in the mantle: *Nature Geoscience*.
- 86 Officer, T., and Secco, R. A., 2020, Detection of high P,T transformational faulting in Fe₂SiO₄ via in-situ acoustic
87 emission: Relevance to deep-focus earthquakes: *Physics of the Earth and Planetary Interiors*, v. 300, p.
88 106429.
- 89 Perrillat, J. P., Chollet, M., Durand, S., van de Moortele, B., Chambat, F., Mezouar, M., and Daniel, I., 2016, Kinetics
90 of the olivine-ringwoodite transformation and seismic attenuation in the Earth's mantle transition zone: *Earth
91 and Planetary Science Letters*, v. 433, p. 360-369.
- 92 Riviere, J., Lv, Z., Johnson, P. A., and Marone, C., 2018, Evolution of b-value during the seismic cycle: Insights from
93 laboratory experiments on simulated faults: *Earth and Planetary Science Letters*, v. 482, p. 407-413.
- 94 Rutter, E. H., and Brodie, K. H., 1988, EXPERIMENTAL SYNTECTONIC DEHYDRATION OF SERPENTINITE
95 UNDER CONDITIONS OF CONTROLLED PORE WATER-PRESSURE: *Journal of Geophysical
96 Research-Solid Earth and Planets*, v. 93, no. B5, p. 4907-4932.
- 97 Schubnel, A., Brunet, F., Hilairret, N., Gasc, J., Wang, Y., and Green, H. W., II, 2013, Deep-Focus Earthquake
98 Analogs Recorded at High Pressure and Temperature in the Laboratory: *Science*, v. 341, no. 6152, p. 1377-
99 1380.
- 00 Syracuse, E. M., van Keken, P. E., and Abers, G. A., 2010, The global range of subduction zone thermal models:
01 *Physics of the Earth and Planetary Interiors*, v. 183, no. 1-2, p. 73-90.
- 02 Turner, H. H., 1922, On the Arrival of Earthquake Waves at the Antipodes, and on the Measurement of the Focal
03 Depth of an Earthquake: *Geophysical Supplements to the Monthly Notices of the Royal Astronomical
04 Society*, v. 1, no. 1, p. 1-13.

05 van Keken, P. E., Currie, C., King, S. D., Behn, M. D., Cagnioncle, A., He, J., Katz, R. F., Lin, S.-C., Parmentier, E.
06 M., Spiegelman, M., and Wang, K., 2008, A community benchmark for subduction zone modeling: *Physics*
07 *of the Earth and Planetary Interiors*, v. 171, no. 1-4, p. 187-197.
08 Wang, Y., Zhu, L., Shi, F., Schubnel, A., Hilairet, N., Yu, T., Rivers, M., Gasc, J., Addad, A., Deldicque, D., Li, Z.,
09 and Brunet, F., 2017, A laboratory nanoseismological study on deep-focus earthquake micromechanics:
10 *Science Advances*, v. 3, no. 7.
11 Wiens, D. A., McGuire, J. J., and Shore, P. J., 1993, EVIDENCE FOR TRANSFORMATIONAL FAULTING
12 FROM A DEEP DOUBLE SEISMIC ZONE IN TONGA: *Nature*, v. 364, no. 6440, p. 790-793.
13 Wiens, D. A., 2001, Seismological constraints on the mechanism of deep earthquakes: temperature dependence of
14 deep earthquake source properties: *Physics of the Earth and Planetary Interiors*, v. 127, no. 1-4, p. 145-163.
15 Yoshioka, S., Torii, Y., and Riedel, M. R., 2015, Impact of phase change kinetics on the Mariana slab within the
16 framework of 2-D mantle convection: *Physics of the Earth and Planetary Interiors*, v. 240, p. 70-81.
17 Zhan, Z., 2020, Mechanisms and Implications of Deep Earthquakes: *Annual Review of Earth and Planetary Sciences*,
18 v. 48, no. 1, p. 147-174.
19 Zhan, Z. W., 2017, Gutenberg-Richter law for deep earthquakes revisited: A dual-mechanism hypothesis: *Earth and*
20 *Planetary Science Letters*, v. 461, p. 1-7.

1 Supplementary Materials for

2
3 **Deep Focus Earthquakes: From High Temperature Experiments to Cold**
4 **Slabs**

5
6 Julien Gasc*, Clémence Daigre, Arefeh Moarefvand, Damien Deldicque, Julien Fauconnier,
7 Blandine Gardonio, Claudio Madonna, Pamela Burnley and Alexandre Schubnel

8
9 *gasc@geologie.ens.fr

10
11
12
13
14
15 **This file includes:**

16 Materials and Methods information
17 Table 1
18 Figures S1 to S4
19 References
20
21

22 MATERIALS AND METHODS

23 Starting Material and Sample Preparation

24 Germanium olivine (Ge-Olivine, Mg_2GeO_4) was synthesized from Mg and Ge oxide powders by
25 repeatedly heating the powders together at 1300°C in a Pt crucible and mixing them in an agate mortar.
26 Excess Ge oxide, with respect to the Ge-olivine stoichiometry, was used in order to insure the presence of
27 ~ 10 vol. % of germanium pyroxene (Ge-Px, $MgGeO_3$) in the resulting powder. The purpose of
28 incorporating Ge-Px is to better image deformation microstructures in the recovered samples, which is
29 difficult to achieve in single phase aggregates due to the lack of contrast. A large cylindrical sample
30 (~ 2.5 cm in diameter and 5 cm long) of Ge-olivine was then sintered from this powder by Hot Isostatic
31 Pressing (HIP) at the ETH of Zurich in a gas apparatus at 200 MPa and 1200°C for 9 hours. Griggs-sized,
32 cylindrical samples of 4.4 mm in diameter by 10 mm in length were then cored in the HIP sample.

33 One of these cores was subsequently fully reacted to Ge-spinel (Mg_2GeO_4 with a modified spinel
34 structure, similar to that of Mg_2SiO_4 ringwoodite) in the new-generation Griggs apparatus at ENS Paris
35 under hydrostatic conditions at 1.5 GPa and 930°C for 6 hours. Two 2.5 mm long cylinders were then sawed
36 from this Ge-spinel core and used in experiment, TF2F, where the Ge-olivine core was only 5 mm long and
37 sandwiched between the Ge-spinel samples.

38 The texture of the starting material, i.e., the synthetic Ge-olivine sinter, and that of the recovered
39 deformed samples was analyzed by Scanning Electronic Microscopy (SEM). Images in backscatter
40 electron mode were collected on all samples and Electron Back Scatter Diffraction (EBSD) maps were
41 collected on the starting material (i.e., the HIP sample). The former allows detailed imaging of
42 deformation microstructures as all three phases present in the recovered samples appear in different
43 shades of gray thanks to their different densities and the latter allows precise characterization of grain size
44 and aspect ratio, phase distribution and crystallographic preferred orientation (CPO). EBSD maps were
45 processed with the help of the MTEX toolbox (Bachmann et al., 2010; Mainprice et al., 2015). Figure S1
46 shows results from an EBSD map analysis, where grain boundaries were assigned with MTEX, thus
47 allowing to visualize grain size and phase distribution. The average Ge-olivine grain size is about

48 ~30 μm . Ge-pyroxene grains are evenly distributed within the Ge-olivine matrix and amount to 6 vol%
49 (Figure S1a). Most Ge-olivine grains have a tabular shape and are slightly elongated (Figure S1b). This
50 typical orthorhombic habitus of olivine usually associates the crystallographic *b*-axis with the shortest
51 dimension of the grains (Miyazaki et al., 2013). Consequently, any shape preferred orientation of the
52 grains induces a CPO of Ge-olivine, which is the case here during compaction of the powder in the
53 canister used for HIP sintering, as the short axis of the grains and therefore the *b*-axis tend to align
54 parallel to the compaction direction (Gasc et al., 2019). This results in slight a CPO dominated by a point
55 maximum of the *b*-axis in the pole figures and an *a*-axis girdle (Figure S1c and d).

56

57 **Deformation Experiments in the New Generation Griggs Rig**

58 High pressure and temperature deformation experiments were performed in a new-generation
59 Griggs type apparatus (Precigout et al., 2018). Full details regarding the whole experimental setup,
60 including acoustics, are available in Moarefvand et al. (2021). The cored samples were encapsulated in Au
61 sleeves closed on both ends with Au disks. The pressure medium consisted in solid NaCl. Resistive heating
62 was generated through a graphite furnace and temperature was monitored with two K-type thermocouples.
63 Some Pb was used between the top of the sample and the alumina piston to cushion the sample during
64 pressurization.

65 All experiments were performed at a constant pressure of 1.5 GPa and constant temperatures
66 ranging between 506 and 843°C, i.e., in the Ge-spinel field. Temperature was ramped to the desired value
67 during compression. The values read on the thermocouples were comprised between 540 and 900°C.
68 However, these values represent an upper bound value, as both thermocouples are positioned closer to the
69 graphite furnace than the sample is. Additional temperature calibration experiments were performed with
70 one of the two thermocouples placed at the center of the cell, where the sample sits during deformation
71 experiments. These calibrations indicate that the difference between the center of the cell and the
72 thermocouple reading can be as high ~ 13 %, which therefore represents a lower bound for the actual mean
73 sample temperature. These uncertainties represent a few tens of degrees and have been reflected on the

74 reported temperatures which were corrected by 6.8 % from the initial thermocouple reading. This is also
75 reported in table 1.

76 After reaching high P-T conditions, the deformation piston was moved by the hydraulic ram using
77 a constant oil flow, which eventually translates to a steady displacement of the piston and a constant strain
78 rate. Axial shortening (i.e., pure shear) was performed at strain rates ranging from 5.0×10^{-6} to $4.3 \times 10^{-}$
79 5 s^{-1} .

80

81 **Mechanical Data Processing**

82 Hit points were determined using a traditional approach, by identifying the intersection between
83 the linear parts of the load-displacement curves corresponding to the run-in (i.e., when the deformation
84 piston is moving through the lead piece) and the elastic loading of the sample (Holyoke and Kronenberg,
85 2010). The alumina piston used to deform the sample has a diameter of 5 mm, whereas the initial diameter
86 of the sample is ~ 4.4 mm. However, due to sample barreling, the sample diameter increases upon axial
87 strain. Therefore, stress was calculated using a surface correction assuming the sample kept a cylindrical
88 shape and a constant volume during axial shortening. The actual surface on which the load of the piston is
89 transmitted thus increases during deformation. It was assumed that this surface cannot exceed a value
90 corresponding to the 5 mm diameter of the piston that transmits the axial load applied.

91

92 **Acoustic Emissions Monitoring**

93 The new generation Griggs rig at ENS is equipped with acoustic emission recording capability.
94 Acoustic Emissions (AEs) were detected with the use of an Olympus® V156 transducer, which has a center
95 frequency of 5 MHz and is polarized for shear wave detection. The transducer was glued under the carbide
96 base plate located under the sample assembly during the experiment. It was glued with epoxy on an alumina
97 disc to isolate it electrically from the press. The signal was amplified at 30 dB and filtered with a low-pass
98 filter, which substantially improves the signal/noise ratio and therefore allows detecting smaller AEs. A
99 threshold level was set above the background noise level in order to trigger AE recording. Waveforms of

100 8192 data points were collected with a sampling frequency of 50 MHz (i.e., the waveforms are 163.84 μ s
101 long) whenever the signal rose above the threshold level. In addition the unamplified and unfiltered signal
102 was also recorded for all AEs. For small AEs, this raw recording does not provide useful information as the
103 signal lies below noise level. For the largest AEs however, for which the amplified signal is saturated, the
104 unamplified signal is not and allows comparing the magnitude of these large events with much smaller
105 ones.

106

107 **Magnitude-Frequency Distributions**

108 The relative amounts of energy radiated by the AEs were assessed by calculating the root mean
109 square (RMS) of the signal for each AE. Arbitrary moment magnitudes, M_w , were then assigned to the AEs
110 based on the RMS values, which scale proportionally with the amount of radiated energy, E_R , of each AE,
111 i.e., $\text{RMS} \propto E_R \propto 10^{M_w}$ (Sammonds et al., 1992). The same trigger level was used in all experiments, which
112 implies that the smallest detected events (right above the noise level) have the same magnitude in all
113 experiments (-8.6); with the exception of TF2F for which the smallest events are larger due to a lesser
114 sensitivity of the transducer. These magnitudes were then used to investigate the magnitude-frequency
115 distribution of the AEs using the conventional Gutenberg-Richter formalism, in which the number of
116 events, N , of magnitude $\geq M_w$ obeys $\log_{10}(N) = a - b \times M_w$ (Gutenberg and Richter, 1949). Thanks to the
117 fractal nature of fault networks, this relation holds from sample- to Nature-sized faults, as attested by the
118 similar b -values obtained in experiments and seismology. Therefore the analysis of b -values yields precious
119 information regarding the mechanisms in the samples that can be up-scaled and are relevant to DFEs in
120 subduction zones The b -values were retrieved from a maximum likelihood estimate (Aki, 1965).

121 Frequency vs magnitude histograms are shown in Figure S3. Experiments BR1F and DU2S, for which
122 seven and no AEs were collected, respectively, do not appear on this figure. Moment magnitude is defined
123 as $M_w \propto \frac{2}{3} \log_{10}(L^n)$, where L is the length of the fault plane (Aki, 1981). Therefore, under constant n ,
124 b -values reflect the fractal dimension of earthquakes, or in the present case, AEs. This fractal dimension,

125 D_H , is partly controlled by the topological dimension of the region where faults propagate, whether it be
126 earthquakes or AEs. Under the standard assumption that $n = 3$, $D_H = 2b$ and the fractal dimension of AEs
127 at 703°C, corresponding to a b -value of ~ 0.7 is $D_H = 1.4$ (Hirata, 1989; Legrand, 2002; Zhan, 2017).
128 Whereas for DU1F at 843°C, $D_H = 3$. The value of $b = 1.1$ retrieved for BR2S at 609°C, has a greater
129 uncertainty due to a lower number of AEs, however, it is consistent with the standard brittle failure observed
130 in the mechanical data (Figure 1). These data show a kink at $M_w \sim 7.6$ in the Gutenberg-Richter relationship,
131 which may be attributed either to a higher completion magnitude than for other experiments or to a shift in
132 b -value during deformation (Riviere et al., 2018).

133

134 **Sample Recovering and Imaging**

135 All deformed samples were recovered within their Au jacket and cut parallel to the shortening
136 direction. Whenever a clear fault offset could be observed through the gold jacket, the cut was performed
137 perpendicular to the apparent fault. These cross sections were mirror-polished by repeatedly polishing the
138 surface with decreasing grit sizes down to colloidal silica (50 nm grain size). The samples were then
139 analyzed by SEM so that the AEs obtained during deformation could be related to reaction progress and
140 deformation microstructures. Images were collected in backscattered electron mode to benefit from the
141 density contrast between Ge-px, Ge-spinel and Ge-olivine.

142

143 **Growth Rates and Kinetics of The Olivine-Ringwoodite Transformation**

144 The transformational faulting window identified in Figure 3 is centered on experiments performed at
145 703°C in the present study. We note that the BR2S data point (609°C) at a growth rate of $2 \times 10^{-11} \text{ m s}^{-1}$
146 corresponds to a few AEs and very limited ductility, which suggests that it lies close to the lower
147 temperature limit of the brittle field. Similarly, the DU1F data point (843°C) at $2.2 \times 10^{-8} \text{ m s}^{-1}$, which,
148 despite the absence of brittle failure generated a large number of AEs, lies close to the upper temperature
149 boundary. The temperature shift of this transformational faulting window between the present results and

150 the ones previously reported is related to the kinetics of the olivine-ringwoodite transformation. In the
151 present work, it is assumed that the reaction kinetic is primarily controlled by growth (and not nucleation)
152 rate of the reaction products. Grain growth, $\dot{\chi}$ in m s^{-1} , is assumed to have the classic temperature
153 dependence:

154

$$155 \quad \ln(\dot{\chi}) = \ln(k_0) - \frac{E_a}{RT} + \ln\left\{T \left[1 - \exp\left(\frac{\Delta G}{RT}\right)\right]\right\} \quad (\text{S1})$$

156

157 , where k_0 is a kinetic constant, E_a is the activation energy in kJ mol^{-1} , R is the universal gas constant in
158 $\text{kJ mol}^{-1} \text{K}^{-1}$ and ΔG in kJ mol^{-1} is the Gibbs free energy change of the reaction at given PT conditions
159 (Perrillat et al., 2016).

160 According to measured grain sizes on the recovered samples, experiments TF1F and TF3S (703°C)
161 yield growth rates of $2\text{-}4 \times 10^{-10} \text{ m s}^{-1}$. Experiment BR2S (609°C) yields $\sim 2 \times 10^{-11} \text{ m s}^{-1}$. Experiment
162 BR1F (506°C) has very little spinel and nucleation barrier might have prevented growth of Ge-spinel grains
163 altogether for most of the experiment; growth rates could not be retrieved from this experiment. For
164 experiments TF3S (703°C), and DU1F and DU2S (843°C) high temperature and/or long durations resulted
165 in high reaction extent. Consequently, grain growth impingement results in underestimating growth rates
166 from final grain sizes. Therefore, growth rates were estimated based on measurements of grain sizes on
167 images of TF1F, TF2F and TF3S and effects of temperature according the growth rate law of Burnley 1995
168 (Burnley, 1995) were used to estimate growth rates for other experiments (i.e., DU1F, BR2S, BR1F and
169 DU2S), based on these measurements.

170 Growth rates for forsterite and fayalite in Figure 3a were calculated using equation (S1) according
171 to Perrillat et al. (2016). The grain growth law reported by Burnley 1995, obtained using similar
172 experiments in a Griggs device (Burnley, 1995) was used for former germanate studies. It was also used to
173 convert the present grain growth values (obtained from measurements on recovered samples) to
174 temperature. We note that this approach predicts larger temperatures than those estimated for our

175 experiments, which implies that the growth rates retrieved are larger than expected from the growth rate
176 law of (Burnley, 1995). This may be explained by a higher water content in our starting material, which
177 was sintered at lower temperature (1200°C) than that of Burnley 1995 (1400°C). Gibbs free energy values,
178 ΔG , of 2 and 4 kJ mol⁻¹ were used for the silicate and germanate systems, respectively. They correspond to
179 equilibrium oversteps of ~0.5 and 1 GPa for Forsterite and Ge-olivine, respectively.

180 Extrapolating to natural strain rates and temperatures, as is done in Figure 3b relies on the activation
181 energy that describes the kinetic-temperature relationship. Experiments on the forsterite end-member had
182 yielded 391 kJ mol⁻¹ (Kubo et al., 2004). However, more recent data on olivine-ringwoodite kinetics have
183 reported lower E_a values of 199-237 kJ mol⁻¹ for silicate olivines with various Fe-Mg ratios (Diedrich et
184 al., 2009; Du Frane et al., 2013; Perrillat et al., 2016). These apparent discrepancies reflect the various
185 chemistry, pressure, temperature and water content used in these studies, which leaves a great uncertainty
186 regarding the actual activation energy. Figure 3b shows the result of an extrapolation using a value of
187 250 kJ mol⁻¹, therefore considered to be a reasonable estimate. Converting $\log(\dot{\chi})$ to equivalent reciprocal
188 temperatures with equation (S1) and plotting them against $\log(\dot{\epsilon})$, yields:

$$189 \log(\dot{\epsilon}) - 4 \cong \log(\dot{\chi}) \quad (S2)$$

190 with a slope of 1 (Figure 3). The slope in the $\log(\dot{\epsilon})$ vs $1/T$ plots in Figure 3 therefore reflects the
191 activation energy of grain growth, E_a , since combining equations S1 and S2 gives $\log(\dot{\epsilon}) \propto \log(\dot{\chi}) \propto E_a/T$.

192

193 **Frictional melting and Fault Propagation in Ge-spinel**

194 A detailed examination of the fault in sample TF2F showed that melt was produced on the fault
195 plane in the Ge-olivine sample, as evidenced by the presence of stretches of fine-grained recrystallized
196 material adjacent to the fault plane (Figure 2c and d). The recrystallization of melt products is expected
197 due to the extremely high cooling rates needed to quench amorphous olivine or spinel glass (Richet et al.
198 1993). Higher magnification images reveal that these regions are composed of small euhedral Ge-olivine
199 grains embedded in a denser matrix (Figure S4 f and g). This microstructure is ubiquitous throughout the

200 whole fault gouge, including next the main fault plane where the pyroxene grains show sharp offsets. In
201 this latter case, however, grain size is even smaller and at the resolution limit of the SEM. Although these
202 features are visualized here in the plane of the image, they have a 3D nature. Since they present important
203 grain size gradients, it is therefore likely that only one of them is intercepted here through its core, where
204 grains are coarser. Ge-olivine grains are embedded in an even smaller grain-sized matrix, the size of
205 which cannot be resolved by SEM (Figure S4g). The high brightness of this matrix in the BSE images
206 suggests that it consists of Ge-pyroxene, consistently with the lower melting point of pyroxene and
207 therefore its later crystallization from the melt and its smaller grain size.

208 In TF2F, the Ge-olivine sample was sandwiched by two Ge-spinel samples of the same diameter, in
209 which the fault also propagated. The fault plane was also examined in the Ge-spinel region (Figure S4).
210 Similarly, the fault is extremely sharp and displays several evidences of frictional melting. We note that
211 this is in agreement with the straightness of the fault across the entire sample, which may reflect fast
212 rupture speed, as expected under high pressure conditions, where mode I crack opening is hindered and
213 thus unable to accommodate high fault tortuosity (Bouchon et al., 2010; Zhan et al., 2015).

214

215 **Conman Simulations**

216 Thermal structures of subduction zones were simulated with the use of Conman 3.0 © (King et al.,
217 2020; King et al., 1990). Thermal profile and velocity of the incoming lithosphere were adjusted to obtain
218 thermal parameters, $\phi = \text{plate age at trench} \times \text{convergence rate} \times \sin(\text{slab dip})$ representing the extreme
219 cases of the Bolivia and Tonga subduction zones (Syracuse et al., 2010). Age plates of 100 and 45 My
220 and velocities of 20 and 6 cm y^{-1} were used for the cases of Tonga and Bolivia, respectively.

221

Experiment	T (°C)	Duration (s)	Volume fraction of Ge-Spinel	Growth Rate (m s^{-1})	Peak Stress (GPa)	Strain Rate at Peak Stress ($\times 10^{-5} \text{ s}^{-1}$)	Mechanical Behavior	Number of AEs	AEs Cumulated RMS (V)	b-value
DU1F	843	13844	0.8	2.2×10^{-8}	1.29	2.79	Ductile	586	1.12	1.5 (0.070)
DU2S	834	54953	0.95	1.7×10^{-8}	1.31	0.495	Ductile	0	0	NA
TF1F	703	9592	0.2	2.6×10^{-10} *	2.15	2.69	Faulting	147	4.55	0.52 (0.042)
TF2F	703	6230	0.05	3.6×10^{-10}	2.23	4.31	Faulting	64	2.00	0.77 (0.095)
TF3S	703	57462	0.2	3.1×10^{-11} *	2.43	0.602	Faulting	633	1.01	0.62 (0.024)
BR2S	609	25449	0.1	2.0×10^{-11} *	2.37	0.998	Faulting	32	1.33	1.1 (0.18)
BR1F	506	7777	0.01	3.8×10^{-14}	2.19	3.54	Faulting	7	0.33	NA

Table T1. Experimental conditions and results. Error on temperature is estimated to be +/- 6.8 %, (see supplementary material on deformation experiments for details). Standard deviation on obtained b-values is given between parentheses.

* Values obtained from grain sizes on recovered samples, other growth rates were inferred from growth rate laws (see supplementary information on growth rates).

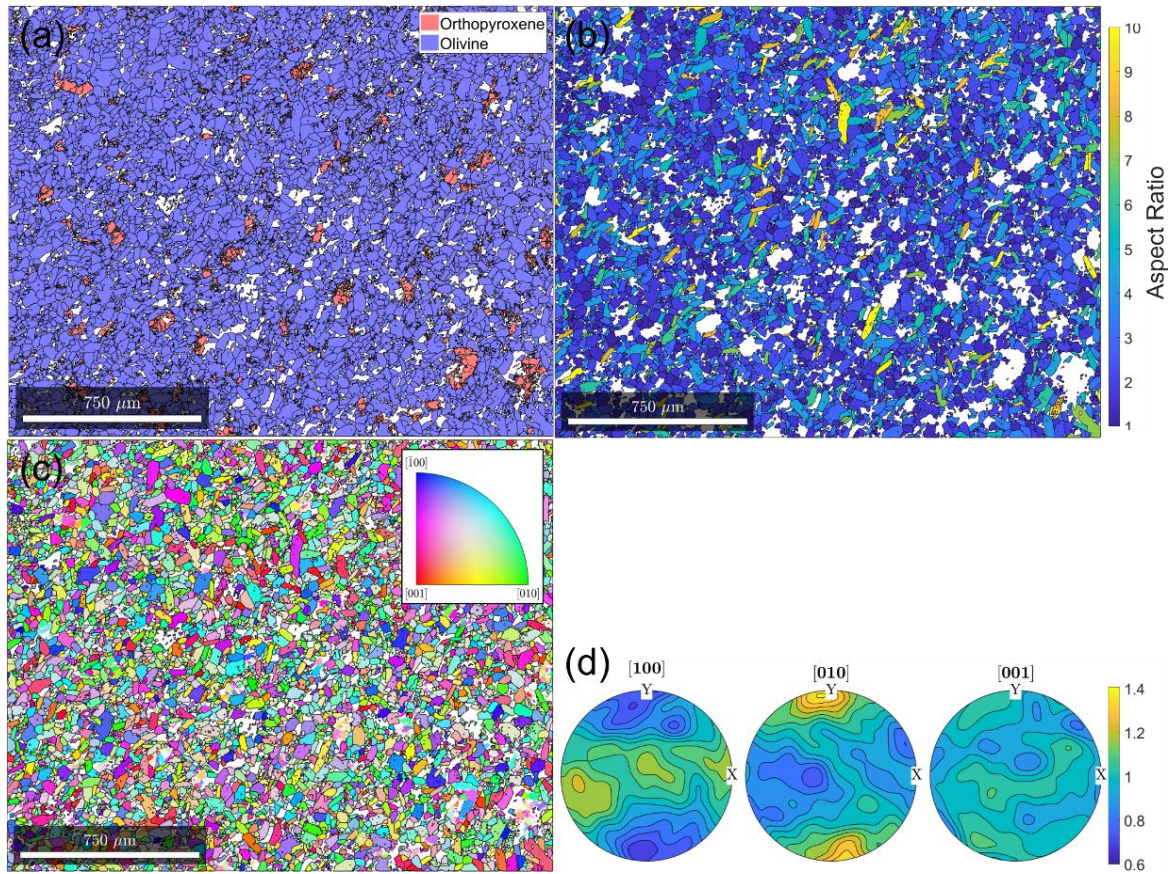


Fig. S1.

Results from EBSD data analysis. (a) Map showing phase distribution and grain boundaries (black contours) of Ge-pyroxene and Ge-Olivine. White represents unindexed pixels due to poor diffraction quality. (b) Ge-olivine grains color coded as a function of their aspect ratio. (c) Map showing the orientation of Ge-olivine grains with in the direction of the long axis of the cylinders used for the experiments (normal to the image plane). Grains are color-coded according to the inverse pole figure in the inset. (d) Pole figures showing the orientation of Ge-olivine grains with respect to the microscope reference frame. The pole figures were rotated 90° here so that the length of the cylinder (i.e., the shortening direction during deformation) is vertical. The color scale corresponds to multiples of average density of crystal axes. Densities were calculated using one point per grain to avoid overrepresentation by larger grains.

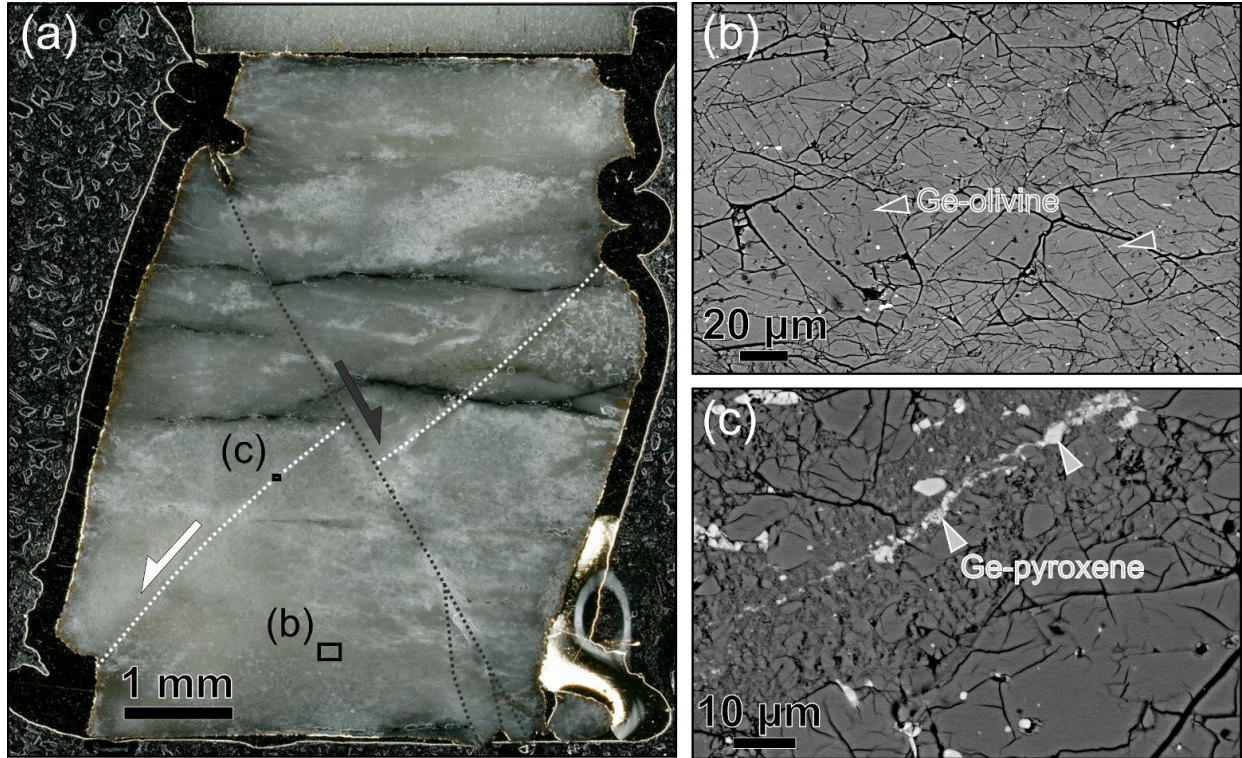


Fig. S2.

Microscopy images of sample BR1F. (a) Optical microscopy image showing the entire sample in its Au capsule. The dashed lines and half-headed arrows indicate the location and the slip direction of two conjugated faults that induced major offsets in the sample. (b) SEM image of the bulk of the sample according to the rectangle in (a). The homogeneous image contrast in BSE mode reveals the absence of Ge-spinel. The initial shape of Ge-olivine grains is still visible (arrow heads); they are heavily fragmented due to the relatively cold temperature of deformation. (c) SEM image of one of the faults according to the rectangle in (a). Shearing of Ge-pyroxene grains (brighter phase) shows the important strain localization that occurred over widths of 10-20 μm . The fault gouge displays a brecciated texture and, unlike for transformational faulting samples, does not contain Ge-spinel.

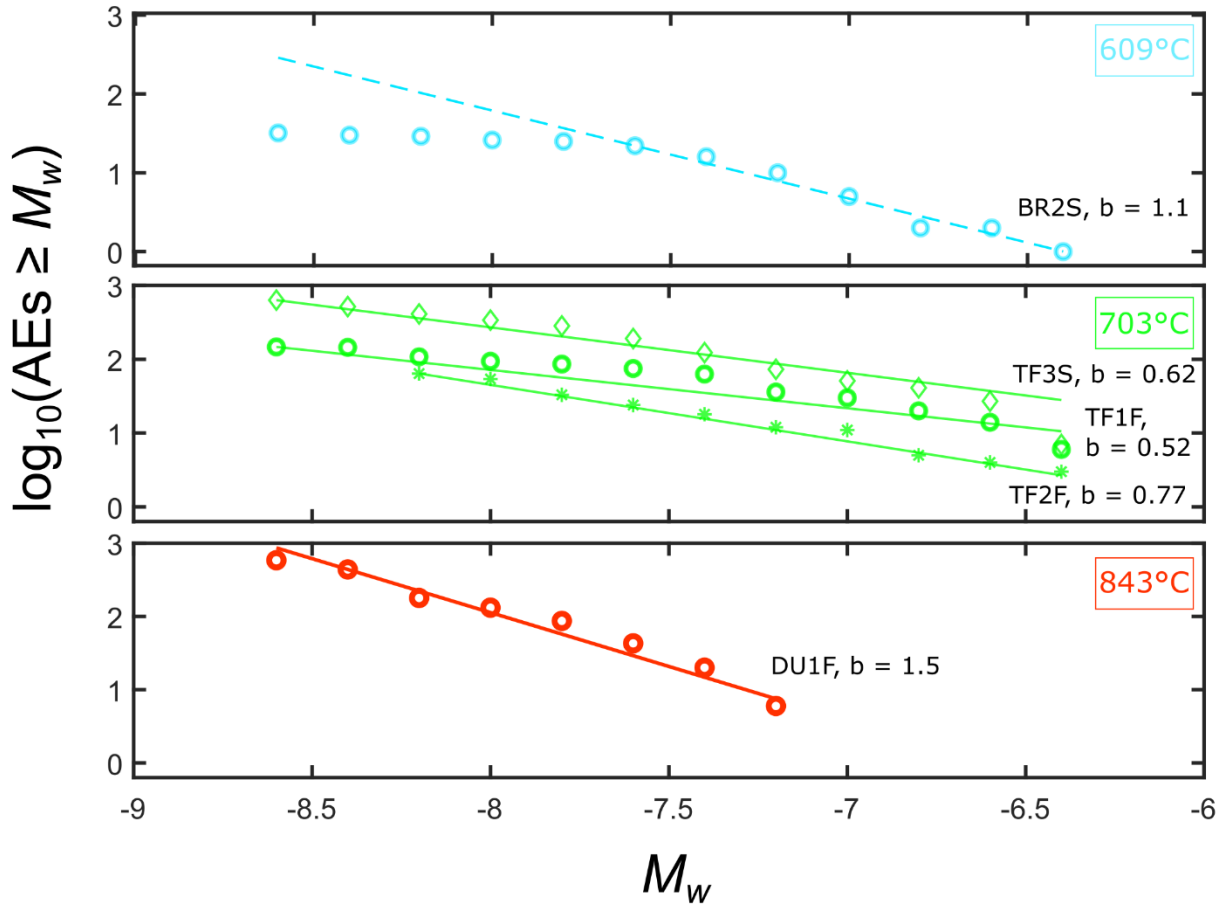


Fig. S3.

Magnitude frequency distribution of AEs and corresponding b -values. Experiment number and associated b -value are provided next to each dataset.

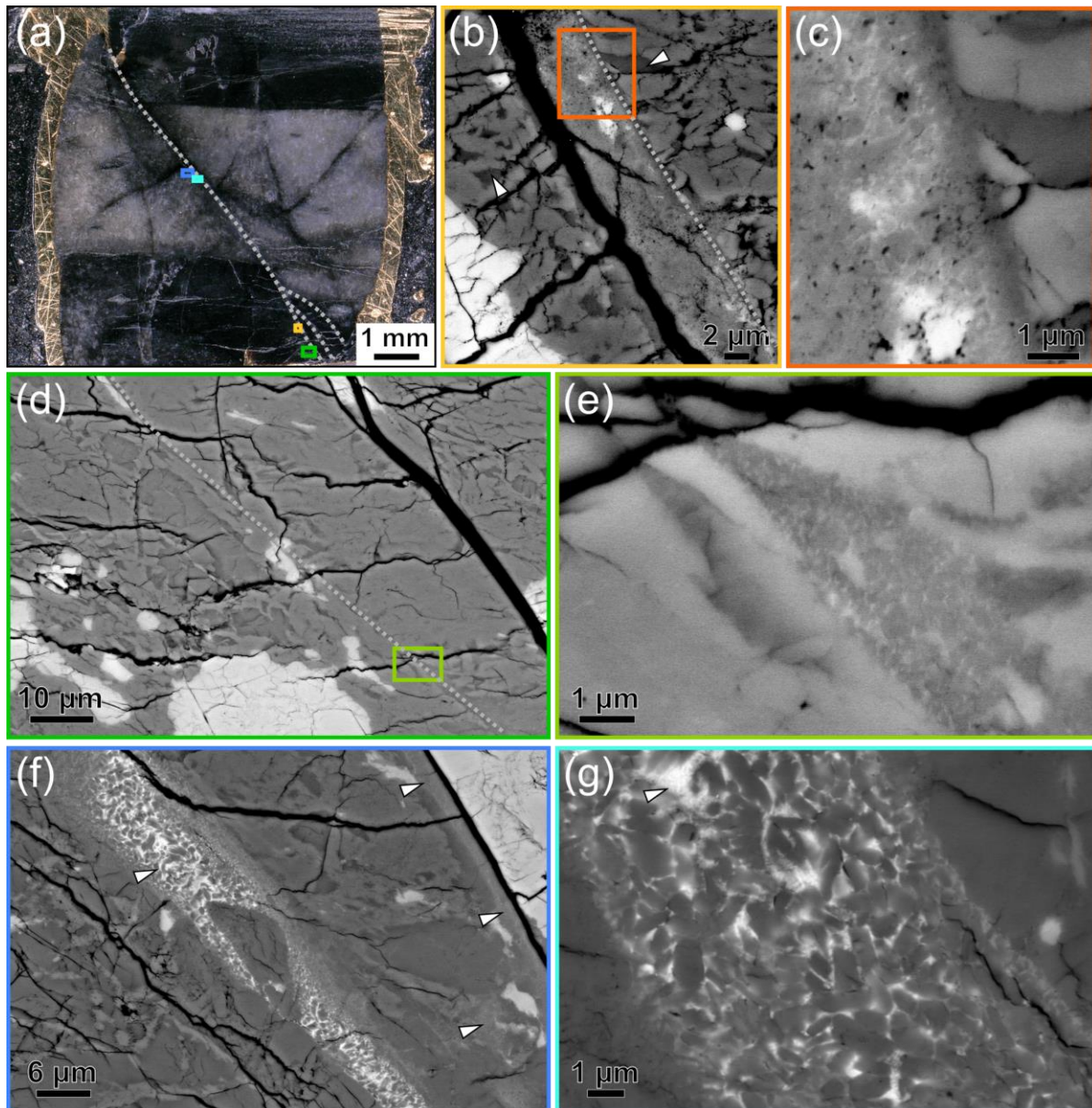


Fig. S4.

Microstructures of sample TF2F. (a) Optical image showing the whole sample. Ge-olivine appears brighter at the center, while the darker regions at the top and bottom of the sample correspond to Ge-spinel. The main fault (dashed lines) propagated through all three parts of the sample. (b)-(e) SEM images of the fault according to the rectangles in (a). (b) The fault, observed here in the bottom Ge-spinel bit, is a few microns wide. Arrow-heads point at remnant Ge-olivine grains. (c) The fault gauge contains an extremely fine-grained texture revealing static recrystallization, typical of quenched melts. (d) Here the fault plane (dashed line) is more discrete with no definable thickness. However, towards the bottom of the image, it widens and forms injectite type features. (e) At high magnification, this feature reveals the same quench texture observed in (c), indicative of frictional melting. (f) Shows a detailed view of the feature described in Figure 2, which reveals that the same quench texture is ubiquitous near the fault plane (arrow-heads) with a smaller grain size. (g) At higher magnification, submicron olivine grains are observed. These are embedded in a denser matrix, composed of nanometric Ge-pyroxene grains (arrow-head).

References

- Aki, K., 1965, Maximum Likelihood Estimate of b in the Formula $\log N = a - bM$ and its Confidence Limits: Bulletin of the Earthquake Research Institute, v. 43, p. 237-239.
- , 1981, A Probabilistic Synthesis of Precursory Phenomena, Earthquake Prediction, p. 566-574.
- Bachmann, F., Hielscher, R., and Schaeben, H., 2010, Texture Analysis with MTEX - Free and Open Source Software Toolbox: Texture and Anisotropy of Polycrystals lii, v. 160, p. 63-+.
- Bouchon, M., Karabulut, H., Bouin, M. P., Schmittbuhl, J., Vallee, M., Archuleta, R., Das, S., Renard, F., and Marsan, D., 2010, Faulting characteristics of supershear earthquakes: Tectonophysics, v. 493, no. 3-4, p. 244-253.
- Burnley, P. C., 1995, The fate of olivine in subducting slabs: A reconnaissance study: American Mineralogist, v. 80, no. 11-12, p. 1293-1301.
- Diedrich, T., Sharp, T. G., Leinenweber, K., and Holloway, J. R., 2009, The effect of small amounts of H₂O on olivine to ringwoodite transformation growth rates and implications for subduction of metastable olivine: Chemical Geology, v. 262, no. 1-2, p. 87-99.
- Du Frane, W. L., Sharp, T. G., Mosenfelder, J. L., and Leinenweber, K., 2013, Ringwoodite growth rates from olivine with similar to 75 ppmw H₂O: Metastable olivine must be nearly anhydrous to exist in the mantle transition zone: Physics of the Earth and Planetary Interiors, v. 219, p. 1-10.
- Gasc, J., Demouchy, S., Barou, F., Koizumi, S., and Cordier, P., 2019, Creep mechanisms in the lithospheric mantle inferred from deformation of iron-free forsterite aggregates at 900-1200 degrees C: Tectonophysics, v. 761, p. 16-30.
- Gutenberg, B., and Richter, C., 1949, Seismicity of the earth and associated phenomena, Princeton, New Jersey.
- Hirata, T., 1989, FRACTAL DIMENSION OF FAULT SYSTEMS IN JAPAN - FRACTAL STRUCTURE IN ROCK FRACTURE GEOMETRY AT VARIOUS SCALES: Pure and Applied Geophysics, v. 131, no. 1-2, p. 157-170.
- Holyoke, C. W., and Kronenberg, A. K., 2010, Accurate differential stress measurement using the molten salt cell and solid salt assemblies in the Griggs apparatus with applications to strength, piezometers and rheology: Tectonophysics, v. 494, no. 1-2, p. 17-31.
- King, S., Raefsky, A., and Hager, B. H., 2020, ConMan version 3.0.0, Zenodo.
- King, S. D., Raefsky, A., and Hager, B. H., 1990, CONMAN - VECTORIZING A FINITE-ELEMENT CODE FOR INCOMPRESSIBLE 2-DIMENSIONAL CONVECTION IN THE EARTH'S MANTLE: Physics of the Earth and Planetary Interiors, v. 59, no. 3, p. 195-207.
- Kubo, T., Ohtani, E., and Funakoshi, K., 2004, Nucleation and growth kinetics of the alpha-beta transformation in Mg₂SiO₄ determined by in situ synchrotron powder X-ray diffraction: American Mineralogist, v. 89, no. 2-3, p. 285-293.
- Legrand, D., 2002, Fractal dimensions of small, intermediate, and large earthquakes: Bulletin of the Seismological Society of America, v. 92, no. 8, p. 3318-3320.
- Mainprice, D., Bachmann, F., Hielscher, R., and Schaeben, H., 2015, Descriptive tools for the analysis of texture projects with large datasets using MTEX: strength, symmetry and components: Rock Deformation from Field, Experiments and Theory: a Volume in Honour of Ernie Rutter, v. 409, p. 251-271.
- Miyazaki, T., Sueyoshi, K., and Hiraga, T., 2013, Olivine crystals align during diffusion creep of Earth's upper mantle: Nature, v. 502, no. 7471, p. 321-+.
- Moarefvand, A., Gasc, J., Fauconnier, J., Baïssset, M., Burdette, E., Labrousse, L., and Schubnel, A., 2021, A new generation Griggs apparatus with active acoustic monitoring: Tectonophysics, v. 816, p. 229032.

- Perrillat, J. P., Chollet, M., Durand, S., van de Moortele, B., Chambat, F., Mezouar, M., and Daniel, I., 2016, Kinetics of the olivine-ringwoodite transformation and seismic attenuation in the Earth's mantle transition zone: *Earth and Planetary Science Letters*, v. 433, p. 360-369.
- Precigout, J., Stunitz, H., Piquier, Y., Champallier, R., and Schubnel, A., 2018, High-pressure, High-temperature Deformation Experiment Using the New Generation Griggs-type Apparatus: *Journal of Visualized Experiments*, no. 134.
- Richet, P., Leclerc, F., and Benoist, L., 1993, MELTING OF FORSTERITE AND SPINEL, WITH IMPLICATIONS FOR THE GLASS-TRANSITION OF Mg_2SiO_4 LIQUID: *Geophysical Research Letters*, v. 20, no. 16, p. 1675-1678.
- Riviere, J., Lv, Z., Johnson, P. A., and Marone, C., 2018, Evolution of b-value during the seismic cycle: Insights from laboratory experiments on simulated faults: *Earth and Planetary Science Letters*, v. 482, p. 407-413.
- Sammonds, P. R., Meredith, P. G., and Main, I. G., 1992, ROLE OF PORE FLUIDS IN THE GENERATION OF SEISMIC PRECURSORS TO SHEAR FRACTURE: *Nature*, v. 359, no. 6392, p. 228-230.
- Syracuse, E. M., van Keken, P. E., and Abers, G. A., 2010, The global range of subduction zone thermal models: *Physics of the Earth and Planetary Interiors*, v. 183, no. 1-2, p. 73-90.
- Zhan, Z., Shearer, P. M., and Kanamori, H., 2015, Supershear rupture in the 24 May 2013 M-w 6.7 Okhotsk deep earthquake: Additional evidence from regional seismic stations: *Geophysical Research Letters*, v. 42, no. 19, p. 7941-7948.
- Zhan, Z. W., 2017, Gutenberg-Richter law for deep earthquakes revisited: A dual-mechanism hypothesis: *Earth and Planetary Science Letters*, v. 461, p. 1-7.